Ultrafast Electron Radiography of Magnetic Fields in High-Intensity Laser-Solid Interactions

W. Schumaker, N. Nakanii, C. McGuffey, C. Zulick, V. Chyvkov, F. Dollar, H. Habara, G. Kalintchenko, A. Maksimchuk, K. A. Tanaka, A. G. R. Thomas, V. Yanovsky, and K. Krushelnick

Phys. Rev. Lett. **110**, 015003 — Published 2 January 2013

DOI: 10.1103/PhysRevLett.110.015003

Ultrafast Electron Radiography of Magnetic Fields in High-Intensity Laser-Solid Interactions

W. Schumaker,[1] N. Nakanii,[2] C. McGuffey,[1,*] C. Zulick,[1] V. Chyvkov,[1] F. Dollar,[1,†] H. Habara,[2] G. Kalintchenko,[1] A. Maksimchuk,[1] K. A. Tanaka,[2] A. G. R. Thomas,[1] V. Yanovsky,[1] and K. Krushelnick[1]

[1]*Center for Ultrafast Optical Science, University of Michigan, Ann Arbor, Michigan 48109, USA*
[2]*Graduate School of Engineering, Osaka University, Osaka 565-0871, Japan*

(Dated: November 19, 2012)

Using electron bunches generated by laser wakefield acceleration (LWFA) as a probe, the temporal evolution of magnetic fields generated by a 4×10^{19} W/cm^2 ultrashort (30 fs) laser pulse focused on solid density targets has been studied experimentally. Magnetic field strengths of order $B_0 \sim 10^4$ T were observed expanding at close to the speed of light from the interaction point of a high-contrast laser pulse with a 10 μm thick aluminum foil to a maximum diameter of ~ 1 mm. The field dynamics were shown to agree with particle-in-cell (PIC) simulations.

PACS numbers: 52.38.Fz, 52.38.Kd, 52.25.Xz, 52.38.-r, 52.70.-m

Strong magnetic fields are well known to be generated by a variety of mechanisms in laser interactions at a solid density plasma-vacuum interface, including the important Biermann battery effect ($\frac{\partial \mathbf{B}}{\partial t} = -\frac{k_B}{e n_e}(\nabla n \times \nabla T)$)[1]. In such interactions, the laser field generates hot electrons which can circulate through the target and spread along the target's surfaces (front and rear), generating an electromagnetic sheath field that expands from the laser focus [2–5]. Furthermore, complex magnetic fields may arise by filamentation of the expanding current sheet [6]. Measurements of such fields have previously been performed using laser-generated proton radiography[7–12], including time resolved measurements of magnetic fields advecting with plasma flows[14–16]. Current laser driven sources of protons[17] are usually produced by target normal sheath acceleration (TNSA) and are non-relativistic, thereby limiting temporal resolution. In contrast, highly relativistic electrons bunches (>100 MeV) generated by laser wakefield acceleration (LWFA)[18–21] typically have durations less than the driving laser pulse (<30 fs) [22, 23] and can be optically synchronized, therefore enabling the observation of faster dynamics in field structures than can be easily preformed with TNSA.

In the interaction of an oblique incidence relativistic intensity laser pulse ($a_0 \gg 1$, where $a_0 = eE_0/m_e c\omega_0$ is the normalized vector potential of the laser field), the particles are heated primarily by a combination of resonance absorption[24] and Brunel absorption [25] to produce relativistic electrons. These electrons propagate throughout the target and into the vacuum, forming expanding sheath fields on the front and rear surfaces. For metal or plasma targets, the net current within the target volume will be approximately zero[26], but fast electrons will be free to propagate in the vacuum near the surface, balanced by a return current just inside the bulk material. This leads to a thin Debye sheath with an electric field perpendicular to the surface and an inductively generated azimuthal magnetic field, both expanding radially at close to the speed of light.

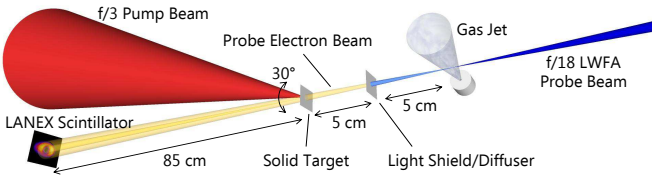

FIG. 1: (color online) Experimental geometry.

In this Letter, we demonstrate proof-of-principle radiography of electromagnetic fields relativistically expanding from the interaction of intense laser pulses with planar, foil targets, using LWFA electron beams. For the experiment, the HERCULES laser (30 fs, 800 nm Ti:sapphire)[27] was operated at 100 TW with native 10^8 contrast ratio between the main pulse and the amplified spontaneous emission (ASE) on the nanosecond pulse pedestal and 10^4 contrast ratio for the picosecond pulse pedestal. The cross-polarized wave (XPW) pulse cleaning technique could be enabled for contrast improvement, yielding up to 10^{11} contrast ratio for the ASE[28]. The experimental geometry is shown in Fig. 1. A pick-off mirror sent the central portion of the beam to an $f/18$ off-axis paraboloid (OAP) mirror focusing the pulse to an intensity of 1.6×10^{19} W/cm^2 ($a_0 = 2.8$) into a He-N_2 (95:5 mass ratio) plasma of 2×10^{19} cm^{-3} peak density above a 1.3 mm supersonic gas jet nozzle, generating a broad energy spectrum electron beam with up to 120 MeV energy and 100 pC charge via ionization injection[29, 30]. The remaining annular beam was sent to a delay stage with 300 ps of adjustable delay and was then focused with an $f/3$ OAP mirror to an intensity of 4×10^{19} W/cm^2 ($a_0 = 4.4$) onto a solid target at 30° incidence. The $f/3$ focus was spatially overlapped on the $f/18$ beam axis 10 cm behind the $f/18$ focus. Timing overlap was achieved using the $f/18$ beam to backlight

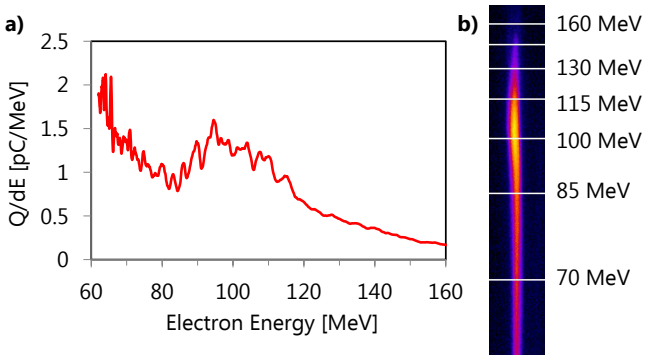

FIG. 2: (color online) (a) Calibrated electron spectrum and (b) spectrometer image for a typical shot.

the breakdown in air at the $f/3$ focus, yielding an optical timing accuracy of ± 30 fs between the two beam paths.

Since the electron beam exits the gas jet plume with a relatively narrow, but elliptical, divergence (<10 mrad) and a large energy spread ($\Delta E/E \sim 100\%$), a 75 μm thick aluminum foil was placed 5 cm behind the gas jet. This acted both as a shield to block any remaining $f/18$ light from interacting with the rear surface of the solid target as well as a diffuser to allow the electron beam to radiograph a larger area of the target while scattering away the low energy (<15 MeV) electrons as $\theta_{scatter} \propto E^{-1}$[31]. After the electron beam probed the solid target, the electron beam profile was measured 85 cm away from the target by a LANEX scintillator screen at 45° to the beam imaged with a CCD camera at 90° to the beam to minimize distortion. Because an accurate electron spectrometer could not be placed behind the solid target, diffuser, and LANEX screen, a charge-calibrated spectrometer with a 0.8 T magnet and LANEX screen was installed directly behind the gas jet and was used to characterize the electron beam energies in a separate shot series. A typical electron spectrum is shown in Fig. 2.

The focal position on the solid target was found by optimizing the X-ray signal with a shielded plastic scintillator coupled to a photomultiplier tube over a number of shots while blocking the $f/18$ beam. Next, the $f/3$ beam was blocked and the electron beam was checked for pointing and charge stability both with and without the diffuser. After optimizing the solid target focus and electron beam, both beams were unblocked and a series of shots were taken while varying the relative time delay of the $f/3$ beam with respect to the $f/18$ beam. The solid target and diffuser were refreshed after each shot and aligned to the optimum focal position. A variety of solid target thicknesses ($10 - 200$ μm) and materials (Al, Cu, Au, and Mylar [$C_{10}H_8O_4$]) were investigated for this experiment, although thin (10-13 μm) targets were primarily used to minimize scattering.

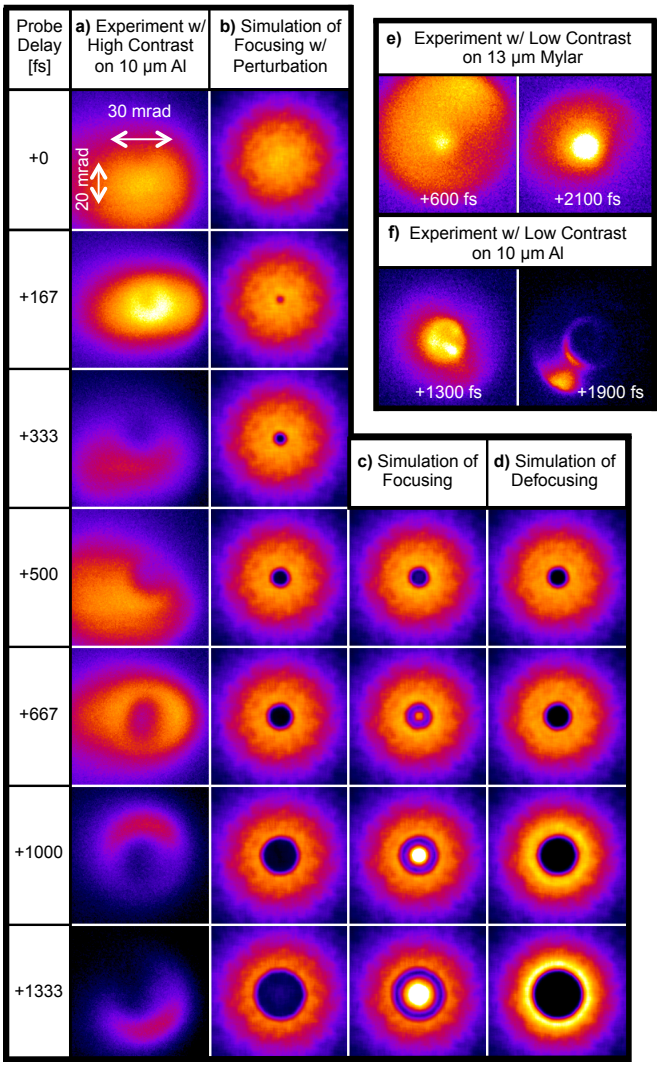

FIG. 3: (color online) (Column a) Measured radiographs taken from laser shots with high contrast and 10 μm Al at delay timings from 0 to +1333 fs. (Columns b-d) Simulated radiographs for each respective delay with defocusing with azimuthal perturbation (b), focusing (c), and defocusing (d). (The color and length scales are the same in each column.) Measured radiographs from low contrast, 13 μm Mylar shots (e) and 10 μm Al shots (f) at selected delays. Note that the electron beam profile is elliptical before interacting with the target and the simulated profiles assume radial symmetry for simplicity.

After passing through the diffuser and target, the electron beam had a Gaussian profile elliptically about the polarization axis with a divergence of $\sim 20 \times 30$ mrad full width at half maximum (FWHM). When the $f/3$ was incident on the target, distinct features were observable, depending on the relative timing $\Delta\tau$, laser contrast level, and the target material. Such features included a focused region of electrons, an area depleted of electrons or a ring structure, and asymmetric structures. Differ-

ences in observed features can be explained by the underlying dynamics of the laser-target interaction since laser contrast and target type (metal vs. dielectric) greatly affect the scale length of the pre-plasma and absorption of laser energy (the details will be elaborated on in a follow-up publication). For low contrast shots (10^8) with Mylar targets, focused structures (Fig. 3(e)) were consistently observed out to 7.5 ps, whereas for aluminum targets (Fig. 3(f)) both could be observed, with holes in the electron beam for longer timescales (>1.5 ps) and focused features appearing for earlier times. With high contrast shots (10^{11}) on 10 μm aluminum, the observed feature was a hole in the electron beam expanding linearly in time (Fig. 3(a)) out to 1.5 ps after an initial period of focusing.

To quantify the size of the high contrast deflection feature while compensating for the irregular probe pointing overlap, the average of four lineouts were taken across the center of deflection region in slices rotated at 45° intervals. For each lineout, the mid-point from the top peak to lowest point of the valley was used to calculate the threshold for the curvature of the feature. A circle was then fit to the feature at this threshold level to find its diameter on the scintillator. Dividing this by the projection magnification (18× in our case, taking the diffuser as the effective source), the diameter of the feature on the target can then be calculated. Fig. 4(d) shows the size of this feature as a function of pulse delay, indicating that the speed of the expansion of the field structure is $(0.98 \pm 0.08)c$. An example lineout for a high contrast shot is shown in Fig. 4(b).

For a radially symmetric azimuthal magnetic field, the probe electron beam will either experience a momentum dependent defocusing or focusing effect, whereas a focusing/defocusing electric field would be radially directed. Since the strongest electric field component is expected to be normal to the target surface and therefore parallel to the electron beam direction, the inductive magnetic field associated with the expanding electric sheath [5] is likely to be the origin of these features. The front surface sheath (facing towards the incident $f/3$ pulse) will generate a magnetic field oriented to focus the probe electron beam, whereas the rear surface sheath (facing towards the probe electron beam) will generate a defocusing magnetic field structure.

To simulate the laser-solid interaction and magnetic field generation, 2D particle-in-cell simulations were run using the OSIRIS 2.0 framework [32]. The charge density profile was constructed piecewise from a rectangle function with exponential ramps on the front and rear surfaces. The peak density ρ_0 was taken as $\rho_0 = 100 n_c$, where n_c is the critical density, the target thickness was $L = 60c/\omega_0$ and the exponential scalelength was $\lambda_{pp} = 6c/\omega_0$. The target was at a 30 degree angle with respect to the simulation box. A Gaussian laser pulse with $a_0 = 6$ was launched in the x_1 direction, linearly

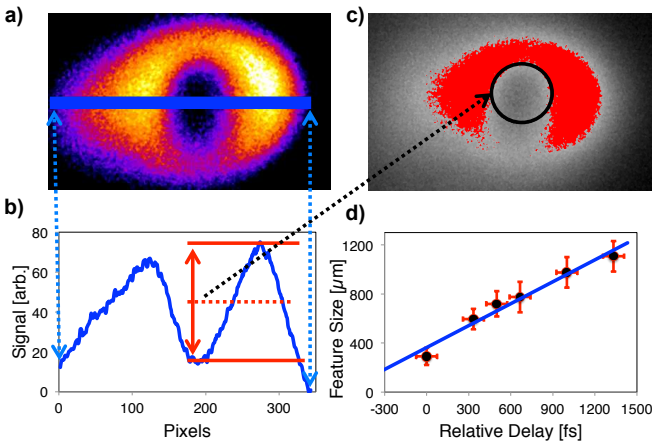

FIG. 4: (color online) (a) Radiograph from Fig. 3(a) with location of lineout. (b) Lineout plot with mid-point between peak-to-valley indicated. (c) Radiograph with threshold set to mid-point and a circle fit to curvature to determine feature diameter. (d) Plot of measured feature size versus delay timing taken from analysis of Fig. 3(a). The error bars represent the variance in determining the diameter over multiple lineouts as well as the timing uncertainty. The linear fit (solid line) indicates that the velocity of the expanding feature is $(0.98 \pm 0.08)c$.

polarized in the x_2 direction with a waist of $w_0 = 40c/\omega_0$ and a 5th order polynomial temporal shape with a duration of $\omega_0 t_0 = 80$.

Two particle species were used; one with charge to mass ratio $q/m = -|e|/m_e$ initiated with a thermal momentum of $p_{th} = 0.01 m_e c$ and one with $q/m = +|e|/m_p$ initiated at rest, where m_p is the proton mass. 9 particles-per-cell were used with a quadratic interpolation charge weighting scheme. The domain was divided by 10000 grid cells in x_1 by 4000 in x_2, yielding cell sizes $\Delta x_1 = 0.1c/\omega_p$ and $\Delta x_2 = 0.2c/\omega_p$. The simulation was run for $\omega_0 t = 1000$ in steps of $\omega_0 \Delta t = 0.07$. Compensated binomial smoothing was applied to fields and currents on the grid.

The simulations indicate that the laser energy is absorbed into a near isotropic population of energetic electrons that propagate through the target and into the vacuum. Within the target volume, background electrons cancel the fast current, but at the interfaces the hot electron density exceeds the background cold electron density. This leads to unneutralized currents in the sheaths at the edges of the targets. A cold return current is drawn from electrons in the higher density region, the net result being oppositely directed currents along the surfaces of the target. The oppositely directed current sheets result in a magnetic field that is approximately a scalelength (λ_{pp}) thickness between them, expanding along the surface at the speed of light (Figure 5). The net result is a relativistically expanding Debye sheath.

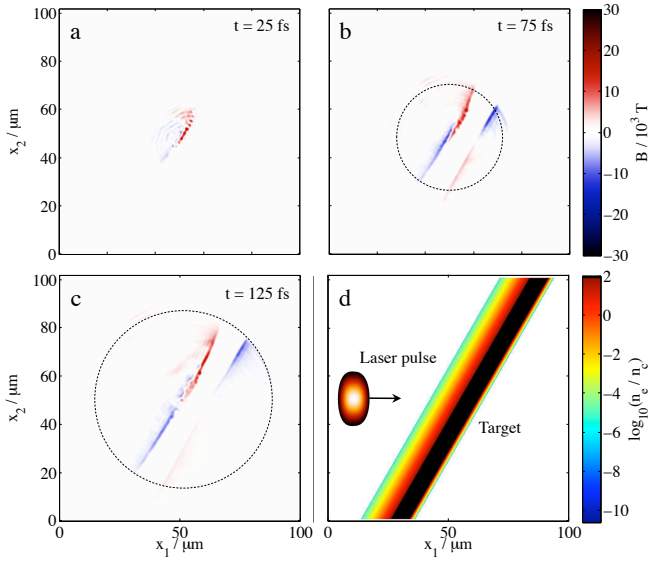

FIG. 5: (color online) (a-c) Magnetic field component in the x_3 direction in Tesla (Fourier filtered to remove the laser field) at different times, where $t = 0$ is when the peak of the pulse is incident on the target surface, and (d) initial electron density profile with initial pulse envelope superimposed.

In this 2D geometry, the electric field is in the simulation plane, normal to the target, and the magnetic field is normal to the simulation plane. For the relativistic electrons moving in the plane of the simulation, these fields exert forces with comparable strength. Hence, due to the geometry, deflections to a probing electron beam normal to the target, as in the experiment, would be expected to be primarily due to the magnetic field. In addition, an electron traveling from the laser focus along the target surface experiences cancellation of the sheath electric force and Lorentz force due to the magnetic field, $\mathbf{F} = -e\mathbf{E} - e\mathbf{v} \times \mathbf{B} \simeq 0$ and can propagate freely.

For a simple model of the generation mechanism, consider a circular loop at radius r about the $\hat{\mathbf{z}}$ axis, normal to the surface near the laser focus, at a distance z_0 from the surface. Assuming azimuthal symmetry about the focal spot, and negligible displacement current normal to the surface, Ampére-Maxwell in integral form will yield $B_\theta(r, z, t) \simeq \frac{1}{c^2 r} \frac{\partial}{\partial t} \int_0^r E_z(r', z, t) r' dr'$. Extending the surface to become a Gaussian 'pillbox' with the second circular surface at $z = 0$, just outside the solid surface where $E_z \simeq 0$, and assuming E_r is negligible, Gauss's law and the continuity equation can be combined to relate the azimuthal magnetic field B_θ to the *radial* fast current j_r as $B_\theta(r, z, t) \simeq -\mu_0 \int_z^\infty j_r(r, z', t) dz'$. Hence in the 2D slab geometry of the simulation, j_r (and therefore B_θ) is approximately constant with r until the electrons are slowed to sub-relativistic speeds, whereas in 3D the j_r (B_θ) would be expected to fall off as $1/r$.

For relativistic electrons generated with a number density $n \sim n_c/4$ in a sheath of thickness $L \sim \lambda_0$, the peak magnitude of the magnetic field generated would be $|B| \sim \mu_0 c|e| n_c \lambda_0/4 \sim 10^4$ T. Such a field cannot indefinitely grow in radius. The maximum field extent at stagnation r_S can be estimated by equating the integrated electromagnetic field energy (falling off as $1/r$) with laser pulse energy U_p having some absorption fraction f (ignoring other dissipative mechanisms and ion motion). Hence, assuming a field of the form $B = B_0 r_0/r_S$ outside radius r_0, the energy absorbed into hot electrons and transferred to the magnetic field is of the order $fU_p \approx 2\pi r_0^2 \ln(r_S/r_0) \lambda_0 B_0^2/\mu_0$. Hence the maximum radius is $r_S \approx r_0 \exp\left(2fU_p/(\pi^3 m_e c^2 n_c r_0^2 \lambda_0)\right)$. For $U_p = 1$ J, $f = 0.2$ and $r_0 = 5$ μm, this gives $r_S \sim 500$ μm, where the field will have dropped to $B \sim 10^2$ T.

This is in reasonable agreement with experimental observations as the deflection of electrons at early times is > 60 mrad, which for a 50 MeV electron yields an integrated field strength of $\sim 10^4$ T·μm. Assuming a sheath of thickness of ~ 1 μm, this level of deflection infers magnetic field strengths of order $\sim 10^4$ T.

To understand the observed electron profiles, a second-order, time-centered electromagnetic particle tracking code was employed. Based on experimental parameters, a flat electron spectrum from 20-120 MeV was modeled with 10^5 particles projected 50 mm with a transverse emittance of $\epsilon_\perp = 53\pi$ mm mrad in a Gaussian distribution. Figures 3(b-d) show simulated electron profiles having passed through a 1 μm thick azimuthal magnetic field structure of the form:

$$B(r,t) = \begin{cases} B_0 & r < r_0 \\ B_0 r_0/r & r_0 \le r \le r_S(t) \\ 0 & r > r_S(t) \end{cases}$$

where $r_0 = 5\mu$m, $r_S(t) = ct$, and $B_0 = 3.8 \times 10^4$ T (corresponding to the PIC simulation output where $f \sim 0.1$). In Fig. 3(d), the magnetic field is defocusing and in Fig. 3(b,c) the magnetic field is focusing. Simulations with both rear and front magnetic fields indicate that they tend to cancel, due to the small scattering angles involved, and hence the resulting deflection of the probe electrons is consistent with a single field corresponding to summation of the front and rear fields.

At early times (small r_S), the electron profile has a void for all magnetic field structures, due to the high field strength causing overfocusing of the electron beam in the focusing cases. For later times (large r_S) as the field strength falls off at the periphery, the difference between focusing and defocusing structures becomes apparent. Although the observed electron profiles in Fig. 3(a) are reminiscent of the defocusing structure, the 10 μm thickness of the target and the short pulse duration make it very unlikely that the rear sheath is stronger than the front – a conclusion that is also supported by particle-in-cell simulations. In Fig. 3(b) the focusing case has also been performed with an azimuthal perturbation to

the field structure (a sinusoidal perturbation, including a radial component to satisfy $\nabla \cdot \mathbf{B} = 0$). This could arise due to filamentation of the current sheet [6], for example. This asymmetry suppresses the focusing of the probe beam and results in a dip in the profile similar to the defocusing case for the relevant timeframe.

In conclusion, electron beams from LWFA can be used as an ultrafast probe of rapidly evolving field structures in laser-plasma interactions. These beams have the advantages of being tunable in energy, having ultra-short duration, and being easily synchronized. In these experiments, the electron spectrum was very broad, which led to some loss of spatial resolution. However, significantly more monochromatic electron beams are achievable from LWFA. Here, such a probe was used to measure fs scale relativistically expanding sheath fields in a laser-solid interaction that extend to diameters of ~ 1 mm and have peak fields of order $\sim 10^4$ T.

The authors would like to acknowledge useful conversations with Prof. F.N. Beg and Dr. R. Stephens. This work was supported by the Department of Energy and the National Science Foundation (Grant No. 0810979). We acknowledge the OSIRIS consortium (UCLA/IST Portugal) for the use of OSIRIS. Simulations were performed on the Nyx Cluster at Univ. of Michigan.

* Current Address: HEDP Group, University of California - San Diego, La Jolla, California 92093, USA

† Current Address: JILA, University of Colorado - Boulder, Boulder, Colorado 80309, USA

[1] L. Biermann, Z. Naturfors. Sect. A-J. Phys. Sci. **5**, 65 (1950), ISSN 0932-0784.

[2] Kolodner P, and Yablomovitch E 1979 Phys. Rev. Lett. **43** 1402

[3] Forslund D W, and Brackbill J U 1982 Phys. Rev. Lett. **48** 1614

[4] P. McKenna, D. C. Carroll, R. J. Clarke, R. G. Evans, K. W. D. Ledingham, F. Lindau, O. Lundh, T. McCanny, D. Neely, A. P. L. Robinson, et al., Phys. Rev. Lett. **98**, 145001 (2007),

[5] C. P. Ridgers, M. Sherlock, R. G. Evans, A. P. L. Robinson, and R. J. Kingham, Phys. Rev. E **83**, 036404 (2011),

[6] F Califano, R Prandi, F Pegoraro, and SV Bulanov. *Phys. Rev. E*, 58(6, Part B):7837, 1998.

[7] Borghesi M, Campbell D H, Schiavi A, Willi O, MacKinnon A J, Hicks D, Patel P, Gizzi L A, Galimberti M, and Clarke R J 2002 *Las. Part. Beams* **20** 269

[8] Li C K, *et al.* Phys. Rev. Lett. **97** 135003 (2006)

[9] Nilson P M, *et al.* Phys. Rev. Lett. **97** 255001 (2006)

[10] Le Pape S, Hey D, Patel P, Mackinnon A, Klein R, Remington B, Wilks S, Ryutov D, Moon S, Foord M *Astrophys. Space Sci.* **307** 341 (2007)

[11] Cecchetti C A, *et al. Phys. Plas.* **16** 043102 (2009)

[12] Willingale L, *et al. Phys. Plas.* **17** 043104 (2010)

[13] Yates M A, van Hulsteyn D B, Rutkowski H, Kyrala G, and Brackbil J U 1982 Phys. Rev. Lett. **49** 1702

[14] Willingale L, *et al.* Phys. Rev. Lett. **105** 095001 (2010)

[15] M. Borghesi, L. Romagnani, A. Schiavi, D. H. Campbell, M. G. Haines, O. Willi, A. J. Mackinnon, M. Galimberti, L. Gizzi, R. J. Clarke, et al., Appl. Phys. Lett. **82**, 1529 (2003), ISSN 00036951,

[16] K. Quinn, P. A. Wilson, C. A. Cecchetti, B. Ramakrishna, L. Romagnani, G. Sarri, L. Lancia, J. Fuchs, A. Pipahl, T. Toncian, et al., Phys. Rev. Lett. **102**, 194801 (2009),

[17] Clark E L, Krushelnick K, Davies J R, Zepf M, Tatarakis M, Beg F N, Machacek A, Norreys P A, Santala M I K, Watts I, and Dangor A E 2000 Phys. Rev. Lett. **84** 670; Maksimchuk A, Gu S, Flippo K, Umstadter D, Bychenkov V Yu 2000 Phys. Rev. Lett. **84** 4108; Snavely R A, *et al.* 2000 Phys. Rev. Lett. **85** 2945

[18] T. Tajima and J. M. Dawson, Phys. Rev. Lett. **43**, 267 (1979),

[19] J. Faure, Y. Glinec, A. Pukhov, S. Kiselev, S. Gordienko, E. Lefebvre, J.-P. Rousseau, F. Burgy, and V. Malka, Nature (London) **431**, 541 (2004), ISSN 0028-0836,

[20] C. G. R. Geddes, C. Toth, J. van Tilborg, E. Esarey, C. B. Schroeder, D. Bruhwiler, C. Nieter, J. Cary, and W. P. Leemans, Nature (London) **431**, 538 (2004), ISSN 0028-0836,

[21] S. P. D. Mangles, C. D. Murphy, Z. Najmudin, A. G. R. Thomas, J. L. Collier, A. E. Dangor, E. J. Divall, P. S. Foster, J. G. Gallacher, C. J. Hooker, et al., Nature (London) **431**, 535 (2004), ISSN 0028-0836,

[22] S. P. D. Mangles *et al.*, Phys. Rev. Lett., **96**, 215001 (2006).

[23] O. Lundh, J. Lim, C. Rechatin, L. Ammoura, A. Ben-Ismail, X. Davoine, G. Gallot, J.-P. Goddet, E. Lefebvre, V. Malka, et al., Nat Phys **7**, 219 (2011), ISSN 1745-2473,

[24] Freidberg, J. P., Phys. Rev. Lett., **28**, 785 (1972).

[25] F. Brunel, Phys. Rev. Lett., **59**, 52 (1987).

[26] A. Bell, J. Davies, S. Guerin, and H. Ruhl, Plas. Phys. Controlled Fusion **39**, 653 (1997), ISSN 0741-3335.

[27] V. Yanovsky, V. Chvykov, G. Kalinchenko, P. Rousseau, T. Planchon, T. Matsuoka, A. Maksimchuk, J. Nees, G. Cheriaux, G. Mourou, et al., Opt. Express **16**, 2109 (2008),

[28] V. Chvykov, P. Rousseau, S. Reed, G. Kalinchenko, and V. Yanovsky, Opt. Lett. **31**, 1456 (2006),

[29] C. McGuffey, A. G. R. Thomas, W. Schumaker, T. Matsuoka, V. Chvykov, F. J. Dollar, G. Kalintchenko, V. Yanovsky, A. Maksimchuk, K. Krushelnick, et al., Phys. Rev. Lett. **104**, 025004 (2010),

[30] A. Pak, K. A. Marsh, S. F. Martins, W. Lu, W. B. Mori, and C. Joshi, Phys. Rev. Lett. **104**, 025003 (2010),

[31] K. Nakamura and P. D. Group, Journal of Physics G: Nuclear and Particle Physics **37**, 075021 (2010),

[32] R. Fonseca, L. Silva, F. Tsung, V. Decyk, W. Lu, C. Ren, W. Mori, S. Deng, S. Lee, T. Katsouleas, et al., in *Computational Science ICCS 2002*, edited by P. Sloot, A. Hoekstra, C. Tan, and J. Dongarra (Springer Berlin / Heidelberg, 2002), vol. 2331 of *Lecture Notes in Computer Science*, pp. 342–351, ISBN 978-3-540-43594-5,